Journal of Materials Chemistry A

COMMUNICATION

View Article Online
View Journal

Cite this: DOI: 10.1039/c8ta02516a

Received 18th March 2018
Accepted 29th May 2018

DOI: 10.1039/c8ta02516a

rsc.li/materials-a

Pseudocapacitive layered birnessite sodium manganese dioxide for high-rate non-aqueous sodium ion capacitors†

Yalong Jiang,[a] Shuangshuang Tan,[a] Qiulong Wei,[*b] Jun Dong,[a] Qidong Li,[a] Fangyu Xiong,[a] Jinzhi Sheng,[a] Qinyou An[a] and Liqiang Mai[*a]

Layered transition metal oxides are promising cathodes for sodium ion capacitors due to their high specific capacity. In this work, we present a layered birnessite sodium manganese dioxide ($Na_{0.77}MnO_2 \cdot 0.5H_2O$) supported by a two-dimensional conductive network (denoted as b-NMO/C) as a cathode for non-aqueous sodium ion capacitor (SIC). The interlayer crystal water and carbon networks promote the ion/electron transport kinetics and overcome the structural instability, leading to largely enhanced electrochemical performance. As a result, the as-synthesized b-NMO/C cathode delivers a capacity of 192 mA h g^{-1} at 0.25C and 43 mA h g^{-1} even at a high rate of 100C. The attained performance is compared favorably with those of state-of-the-art Mn-based cathodes for sodium ion storage. Furthermore, the assembled asymmetric SIC (b-NMO/C//graphite) exhibits the highest energy (91 W h kg^{-1} achieved at ~84 W kg^{-1}) and power (5816 W kg^{-1} achieved at ~37 W h kg^{-1}) densities within the voltage range of 0.5–3.8 V.

Sodium storage technologies have garnered immense attentions as potential substitutes to lithium ion batteries (LIBs) owing to the low cost and abundance of sodium resources compared to lithium. However, the large mass and radius size of Na ion lead to sluggish diffusion kinetics and large volume expansion during Na^+ intercalation into the host material, resulting in inferior rate capability and cycling stability of sodium storage. As proposed by Conway and Dunn *et al.*,[1,2] pseudocapacitance, especially intercalation pseudocapacitance, delivers a high battery-level capacity accompanied by fast charge storage without undergoing a phase change process. Considering this advantage, most recently, sodium ion capacitors (SICs), usually consisting of a battery/pseudocapacitor-type anode and capacitor-type cathode, are identified and are regarded as promising candidates for next-generation energy storage devices with high energy and power densities and low-cost.[3–8] So far, most reported SICs have focused on pseudocapacitive anodes, such as Nb_2O_5,[3] TiO_2,[4] and $NaTi_2(PO_4)_3$,[5] while activated carbon (AC) was usually used as the cathode. However, electric double layer capacitive AC cathodes deliver an inadequate capacity (30–60 mA h g^{-1}) owing to the limited adsorption of ions on the surface.[9] The development of pseudocapacitive sodium storage cathodes can largely enhance the capacity and energy density of SICs, but not much attentions have been paid to the search for pseudocapacitive cathode materials for SICs.

Layered transition metal oxides, such as $LiMO_2$ (M = Ni, Co or Mn), provide two-dimensional channels for Li ion intercalation and storage and are the dominant cathodes for LIBs to date.[10] Similarly, sodium ions can electrochemically intercalate/deintercalate into/from the layered materials reversibly as first reported in the early 1980s.[11] Layered $NaFeO_2$, $NaCoO_2$, $NaCrO_2$, $NaMnO_2$, $Na[Fe_{1/2}Mn_{1/2}]O_2$ and so forth have been developed in the past decade, exhibiting enhanced electrochemical sodium ion storage performance.[12–14] Among these, the studies on earth abundant and low-cost transition metals (Mn and Fe) are more promising for large-scale application.[15] For example, $Na_{0.6}MnO_2$ showed a capacity of 140 mA h g^{-1} at 2–3.8 V.[16] Most recently, Billaud *et al.*[17] reported a different phase (β-$NaMnO_2$) as the cathode for the first time, which delivered an enlarged capacity of 190 mA h g^{-1} at a rate of C/20 and good rate capability (with a capacity of 142 mA h g^{-1} at 2C). Layered P2-$Na_x[Fe_{1/2}Mn_{1/2}]O_2$ delivered a high reversible capacity of 190 mA h g^{-1} in the voltage range of 1.5–4.2 V.[18] However, owing to the multiple phase transformation processes and sluggish kinetics of ions/electrons, the rate capability and cycling stability of the reported layered cathode materials for sodium ion storage are not satisfactory and still need further improvements.

To enhance sodium ion storage performance, an effective strategy is to enlarge the layer spacing for the facile Na^+ ion diffusion.[19,20] For example, the hydrated vanadium oxide xerogel with nanoconfined fluid water had a large layer spacing of 12.3

[a]State Key Laboratory of Advanced Technology for Materials, Synthesis and Processing, International School of Materials Science and Engineering, Wuhan University of Technology, Wuhan 430070, China. E-mail: mlq518@whut.edu.cn

[b]Department of Materials Science and Engineering, University of California Los Angeles, Los Angeles, CA 90095-1595, USA. E-mail: qlwei@ucla.edu

† Electronic supplementary information (ESI) available: X-ray diffraction, cyclic voltammetry, morphology characterization, coulombic efficiency, and energy dispersive X-ray spectroscopy. See DOI: 10.1039/c8ta02516a

Å, and it delivered enhanced sodium storage performance compared to α-V_2O_5.[19] It was found that the interlayer structure water led to a "shielding effect", which facilitated the solid-state diffusion of large intercalated ions (such as Na^+, Mg^{2+} and Zn^{2+}), reduced charge transfer resistance at the interface and improved the flexibility of the structure during intercalation/extraction.[19,21–24] Similar to the vanadium oxide xerogel structure, another classic example is birnessite manganese dioxide (MnO_2). Normally, birnessite MnO_2 is synthesized by low-cost and facile co-precipitation of potassium permanganate and manganese sulfate in water. In this process, the obtained material consists of interlayer cations and crystal waters in between the MnO_2 layers, denoted as $X_mMnO_2 \cdot nH_2O$, where X represents a kind of cation, such as Na^+, K^+ and Zn^{2+}.[25,26] Remarkably, birnessite MnO_2 has been well studied as the pseudocapacitive electrode in aqueous systems, where the pseudocapacitance arising from fast faradaic redox reactions yields great potential for delivering fast charge–discharge rates.[2,27–29] However, to date, there have been few studies on non-aqueous sodium-based systems, which are capable of delivering higher out-put voltages and thus higher energy density. Previous studies have shown that hydrated layered materials can deliver stable performance in non-aqueous systems.[19,21,30] Meanwhile, the interlayer crystal water was suggested to enhance the kinetics of the charge storage process. Thus, realizing the pseudocapacitive charge storage of low-cost layered birnessite $Na_mMnO_2 \cdot nH_2O$ (denoted as b-NMO) in non-aqueous systems is promising to deliver both high-rate and high-energy sodium ion capacitors, which has not been reported yet.

Herein, we develop a low-cost wet-chemical method to synthesize layered $Na_{0.77}MnO_2 \cdot 0.5H_2O$ supported by two-dimensional carbon conductive networks, named b-NMO/C. As a sodium storage cathode, the b-NMO/C displays much enhanced rate performance compared to the b-NMO and the heat-treated b-NMO/C (b-NMO/C-HT) samples. Systematic characterization and detailed kinetic analyses were undertaken to investigate the charge storage mechanism, which was demonstrated as a pseudocapacitive reaction. Benefiting from the introduction of interlayer crystal water and the modified electronic conductivity, the b-NMO/C cathode delivers remarkable electrochemical performance. As a result, it delivers a capacity of 192 mA h g^{-1} at 0.25C (1C = 200 mA g^{-1}). Even at high rates of 10, 40 and 100C, a high capacity of 102, 70 and 43 mA h g^{-1} is achieved, respectively. Further, the assembled b-NMO/C//graphite SIC delivers a maximum energy density of 91 W h kg^{-1} at a power density of 84 W kg^{-1}. When the power density is increased to 5816 W kg^{-1}, the energy density is 37 W h kg^{-1}.

The layered b-NMO/C was synthesized by a facile low-cost co-precipitation method in a water bath.[30–32] Briefly, carbon nanotubes (CNTs) and Ketjenblacks (KBs) were first dispersed in a manganese(II) nitrate solution by ultrasonic treatment. Then, the mixed solution of hydrogen peroxide and sodium hydroxide was added dropwise into the above solution. The resultant solution was then heated in a water bath at 50 °C for 24 hours to obtain the layered b-NMO/C. The layered birnessite framework consists of a two-layer hexagonal unit cell with a space group of $P6_3/mmc$ (Fig. 1a).[33] As shown in Fig. 1a, the layered b-NMO structure supported by the CNT & KB conductive networks can provide effective ion/electron transport. The morphology of the hybrid structure is further shown in the scanning electron microscopy (SEM) image (Fig. 1b). The as-synthesized b-NMO without adding conductive additives and b-NMO/C-HT with additional heat-treatment at 400 °C in argon were prepared to investigate the roles of conductive additives and crystal water. Both control samples show the nanosheet morphology (Fig. S1 and S2†).

The powder X-ray diffraction (XRD) patterns of the as-synthesized b-NMO/C, b-NMO and b-NMO/C-HT were collected to determine their crystallography. All samples (Fig. 1c) show the typical (00*l*) reflection peaks of the layered birnessite structure. The diffraction peak observed at 26.5° comes from the CNTs, indicating that the pre-added conductive additives have no influence on the crystallinity of the synthesized materials. The (002) diffraction peak is attributed to the layer-to-layer distance. Calculated from the XRD results, the b-NMO/C and b-NMO samples have the same layer distances of 7.25 Å. The thermogravimetric (TG) curves of b-NMO (Fig. S3a†) exhibits an obvious weight loss of ~7.9%, corresponding to the loss of crystal water.[34] The b-NMO/C-HT sample shows a slightly decreased layer distance of 7.16 Å, owing to the loss of crystal water from the interlayers after heat-treatment (Fig. S3b†). The structure was further confirmed with the FTIR spectra (Fig. 1d). The peaks centred at 480 and 515 cm^{-1} are the characteristic FTIR bands of birnessite.[35,36] The peak centred at 600 cm^{-1} for b-NMO/C-HT is due to the increase of crystallization degree after heat-treatment.[35] The absorption bands at 1631 and 3421 cm^{-1} for the three samples are attributed to the stretching and bending modes of O–H vibrations and water in the more disordered cases, which confirms the intercalation of crystal water molecules into the layers.[35–37] Furthermore, an inductively

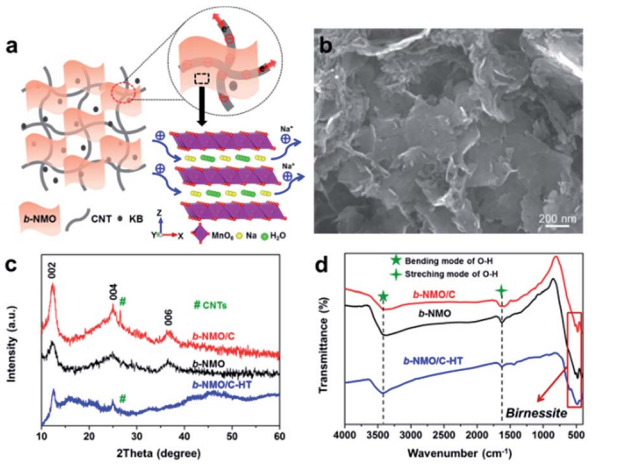

Fig. 1 (a) Schematic of layered b-NMO supported by the CNT & KB conductive networks, intimate contact between the layered b-NMO and CNT & KB conductive networks facilitating charge transport and Na^+ intercalation within the b-NMO layer structure. (b) SEM image of the b-NMO/C. XRD patterns (c) and FTIR spectra (d) of the b-NMO/C, b-NMO and b-NMO/C-HT, respectively.

coupled plasma-atomic emission spectrometry (ICP-AES) analysis shows that the atomic ratio of Na : Mn in layered b-NMO is 0.77 : 1 (Table S1†). X-ray photoelectron spectroscopy (XPS) measurements were carried out to determine the chemical composition (Fig. S4†). The proportion of different oxidation states of the manganese in b-NMO/C was investigated (Table S2†).[38] It is found that the average valence state of b-NMO/C was about +3.24, which was close to the valence state of Mn in $Na_{0.77}MnO_2 \cdot 0.5H_2O$. Based on the above results, the chemical formula of the as-synthesized layered b-NMO is identified as $Na_{0.77}MnO_2 \cdot 0.5H_2O$.

Determined from the CHN elemental analysis (Table S3†), the carbon content of b-NMO/C is 8.09%. The Raman spectrum of b-NMO/C (Fig. S5†) exhibits the characteristic signatures located at around 1350 and 1600 cm^{-1} which are attributed to the D-band (originating from disordered carbon) and G-band (graphitic carbon),[39] respectively, from the existence of CNTs and KBs. Furthermore, the Brunauer–Emmett–Teller (BET) specific surface areas of the b-NMO/C and b-NMO are 26.0 and 0.4 $m^2\ g^{-1}$, respectively. The enlarged surface of the b-NMO/C mainly comes from the existence of the carbon additives, as calculated in the ESI.† Fig. 2a shows the transmission electron microscopy (TEM) image of the b-NMO/C sample, which confirms the nanosheet morphology. The b-NMO nanosheets (b-NMO NSs), CNTs and KB particles are observed. The high resolution transmission electron microscopy (HRTEM) image of a curled edge shows clear layered fringes, and the thickness of the nanosheet is determined to be ~10 nm (Fig. 2b). The measured layer spacing from the HRTEM image is a little smaller than the value calculated from the XRD results, which is possibly because the edge-side was not vertical, and the hydrated composite was easily reduced by strong electron beams in a high vacuum.[40] In addition, Fig. 2b shows the linear fringes of the CNTs (as marked in the orange region) with a spacing of ~3.4 Å, which is consistent with the d_{002} spacing of carbon nanotubes (Fig. S6†).[41] The detailed morphology observations indicate that the b-NMO nanosheets are in good contact with the carbon networks. Energy dispersive X-ray spectroscopy (EDS) elemental mappings (Fig. 2c) were collected as well. They show the homogeneous distribution of Na, Mn, O and C in the b-NMO/C composite, confirming that the conductive carbon networks support the b-NMO nanosheets to realize continuous electron transport. The control sample (b-NMO) shows similar characteristics of the layered birnessite structure (Fig. S1†).

The electrochemical properties of the samples were investigated by assembling coin-type (2016 type) half-cells. Fig. 3a shows the load curves of the layered b-NMO/C cathode measured at a specific rate of 0.25C (50 mA g^{-1}). The charge and discharge curves of b-NMO/C exhibit small hysteresis, indicating the high reversibility of sodium insertion/extraction. The half-cell was firstly charged (Na^+ extraction from the layers) and then followed by repeated Na^+ intercalation and extraction processes. The layered b-NMO/C delivers an initial charge capacity of 125 mA h g^{-1} (Fig. S10a†), indicating that ~0.57 mol Na^+ per formula is extracted from the layers. The related calculations are based on the equation $n = (3.6MC)/F$, where n represents the inserted ion amount, F is the Faraday constant, C is the capacity, and M is the molecular weight.[19,42] The subsequent reversible discharge capacity is 192 mA h g^{-1}, corresponding to an intercalation of ~0.8 Na^+ per formula. Therefore, the sodium storage process is proposed as follows:

$$Na_{0.77}MnO_2 \cdot 0.5H_2O \rightarrow Na_{0.2}MnO_2 \cdot 0.5H_2O + 0.57Na^+ + 0.57e^- \quad (1)$$

$$Na_{0.2}MnO_2 \cdot 0.5H_2O + xNa^+ + xe^- \leftrightarrow Na_{0.2+x}MnO_2 \cdot 0.5H_2O\ (0 < x < 0.8) \quad (2)$$

Ex situ XRD was performed to further investigate the layered structure changes during the charge and discharge processes. The XRD patterns of the electrodes at different reaction states show only slight shifts of the (002) and (004) diffraction peaks, indicating a reversible reaction process without phase changes

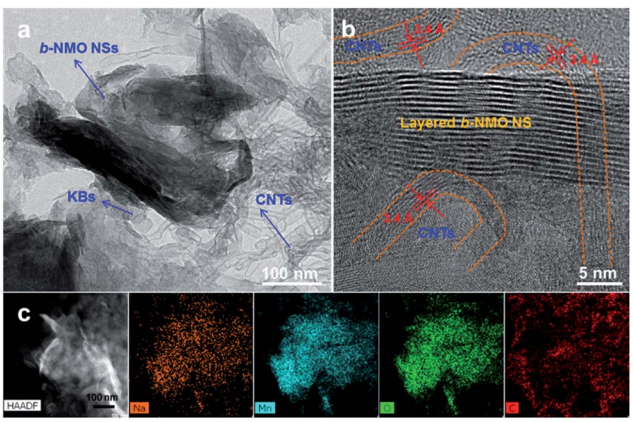

Fig. 2 (a) TEM image of the b-NMO/C, the blue arrows refer to CNTs, KBs and b-NMO NSs. (b) HRTEM image of the b-NMO/C, showing the fringes of the layered b-NMO NS and CNTs, indicating that the b-NMO NS is supported by CNT networks. (c) The EDS elemental mappings of the b-NMO/C, showing the uniform distribution of Na, Mn, O and C.

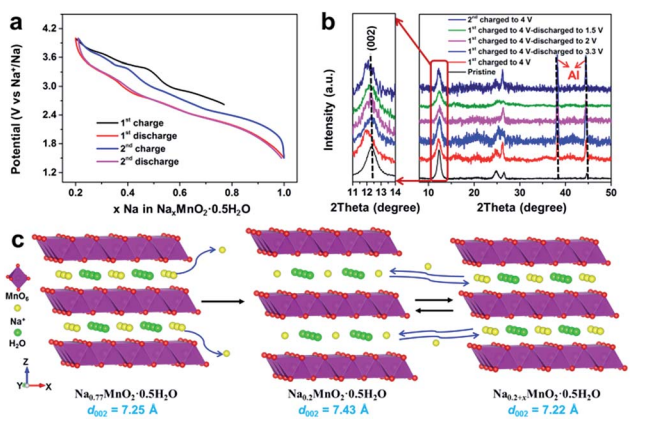

Fig. 3 (a) Load curves of b-NMO/C, corresponding to electrochemical Na extraction and reinsertion. (b) *Ex situ* XRD patterns of the b-NMO/C at various sodiation and desodiation states. (c) The changes of the crystal structure for the birnessite $Na_mMnO_2 \cdot nH_2O$ during Na^+ ion intercalation/extraction.

(Fig. 3b). In detail, the (002) diffraction peak shifts from 12.20° to 11.96° after sodium extraction from the layers (charged to 4 V *vs.* Na^+/Na), indicating that the layer spacing increases from 7.25 to 7.39 Å. The enlarged layer spacing occurs from the extraction of sodium which increases interlayer repulsion. Similar phenomena were observed in vanadium oxide xerogels.[15] After full sodium re-insertion into the interlayers (discharged to 1.5 V *vs.* Na^+/Na), the layer spacing reduced to 7.22 Å, smaller than that in the pristine state (7.25 Å) since more Na^+ ions are stored in the layers. The total lattice expansion between the birnessite-type layers is just ~2.4%, and the lattice breathing is highly reversible (Fig. 3c). It has been demonstrated that the crystal water in between the layers effectively releases the strain caused by the insertion and extraction of Na^+.[2,19,20] Furthermore, the HRTEM images and EDS elemental mappings confirm that the layered structure and the nanosheet morphology are well maintained after cycles (Fig. S7†).

Kinetic analyses were further used to investigate the sodium storage behavior. The cyclic voltammetry (CV) curves of b-NMO/C, b-NMO and b-NMO/C-HT measured at various scan rates (from 0.2 to 10 mV s^{-1}) are shown in Fig. 4a–c and S8a–c.† The redox peaks of the b-NMO/C cathode exhibit the smallest shifts with increasing scan rates among the three samples, indicating the smallest polarization and fastest reaction kinetics. A more detailed relationship between peak current (i) and. scan rate (v) can be elucidated using eqn (3) as shown below:[4]

$$i = av^b \tag{3}$$

The value of $b = 0.5$ indicates semi-infinite linear diffusion-controlled charge storage, while $b = 1$ means capacitive-dominated charge storage.[4] Fig. 4d exhibits the plots of log(i) *versus* log(v) from 0.2 to 1 mV s^{-1} for both cathodic and anodic peaks of three samples. After linear fitting, the b values of layered b-NMO/C are 0.96 and 0.98 for anodic and cathodic peaks, respectively, which are larger than the value of 0.87 and 0.85 for b-NMO and 0.83 and 0.82 for b-NMO/C-HT, suggesting that the layered b-NMO/C displays the fastest reaction kinetics compared to b-NMO and b-NMO/C-HT. Meanwhile, the b values of the b-NMO/C are ~1, indicating a capacitive-dominated charge storage behavior.[4]

As proposed by Dunn and co-workers,[2,4,43] it is possible to further distinguish the diffusion and capacitive contribution towards charge storage from the CV curves. The measured current (i) at a fixed potential (V) can be separated into capacitive effects (k_1v) and diffusion-controlled contributions ($k_1v^{1/2}$) (eqn (4)) to quantitatively characterize the capacitive contribution of each part.

$$i\,(\mathrm{V}) = k_1v + k_2v^{1/2} \tag{4}$$

Fig. 4e shows the capacitive contributions to the charge storage of the b-NMO/C, b-NMO and b-NMO/C-HT at different scan rates, respectively. All three samples show the capacitive contributions to the total charge storage. At a scan rate of 0.2 mV s^{-1}, the capacitive contribution of the b-NMO/C is 72.1%, which is higher than those of the b-NMO (64.2%) and b-NMO/C-HT (47.3%). The BET surface areas of both b-NMO/C (26 $m^2\,g^{-1}$) and b-NMO (0.4 $m^2\,g^{-1}$) are very small, and thus the capacity from the double layer contribution (usually 10 μF cm^{-2}) can be ignored, indicating a dominated pseudocapacitance for the b-NMO/C.[44] The integrated capacitive charge storage of b-NMO/C is ~85.6% at 1 mV s^{-1}, larger than those of b-NMO (80.2%) and b-NMO/C-HT (66.8%), indicating the superior pseudocapacitance of b-NMO/C for rapid charge storage.

Electrochemical impedance spectroscopy (EIS) measurements were further conducted, and the results are shown in Fig. S9a.† The Nyquist plots are composed of a depressed semicircle (characteristic of charge transfer resistance) in the medium-frequency region followed by an oblique line (characteristic of ion diffusion resistance) in the low-frequency region.

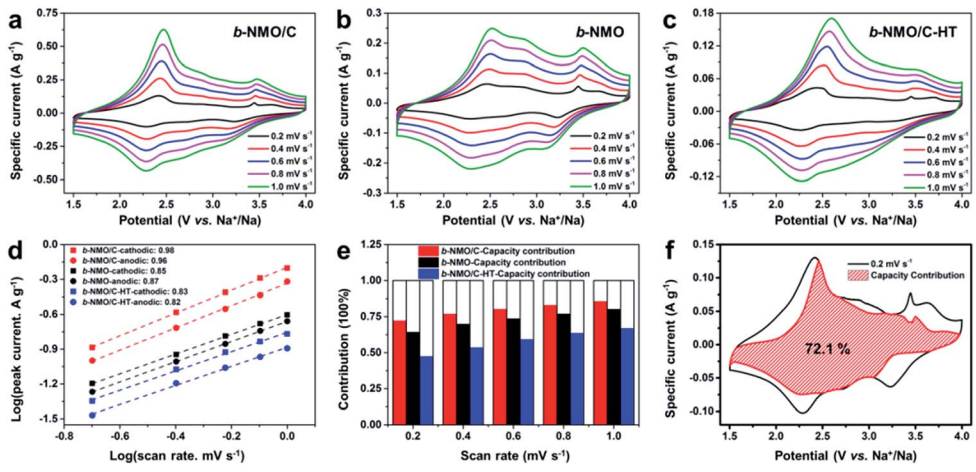

Fig. 4 (a–c) CV curves of the b-NMO/C (a), b-NMO (b) and b-NMO/C-HT (c) at various scan rates from 0.2 to 1 mV s^{-1}, respectively. (d) The normalized peak current *vs.* scan rate plots to determine the b-value for both cathodic and anodic peaks of the b-NMO/C, b-NMO and b-NMO/C-HT. (e) Capacitive contributions to the charge storage of the b-NMO/C, b-NMO and b-NMO/C-HT at different scan rates. (f) Capacitive contributions (shaded area) to charge storage of the b-NMO/C at a scan rate of 0.2 mV s^{-1}.

The charge transfer resistance (R_{ct}) of b-NMO/C (20 Ω) is smaller than those of b-NMO (29 Ω) and b-NMO/C-HT (46 Ω), indicating that the conductive networks of b-NMO/C provide more efficient ion/electron transport than those of the b-NMO and b-NMO/C-HT. The angle of the oblique line in the low frequency region for the b-NMO/C and b-NMO is much larger than a typical semi-diffusion angle of 45°, which is similar to the results obtained in aqueous systems,[28,29,45] indicating that the charge storage is not limited by the diffusion-controlled process. Additionally, the simulations of the Warburg factor (σ) further indicate the enhanced Na^+ ion diffusion ability of b-NMO/C compared to the two other samples (Fig. S9b†).[46]

Based on the detailed investigations of the *ex situ* XRD results and reaction kinetics during sodiation/desodiation processes, a typical pseudocapacitive sodium storage mechanism of b-NMO in a non-aqueous system has been demonstrated. Compared to the b-NMO/C-HT ($Na_{0.77}MnO_2 \cdot 0.18H_2O$/C), the b-NMO/C ($Na_{0.77}MnO_2 \cdot 0.5H_2O$/C) has an increased amount of crystal water in between the layers and exhibits a much higher b value and lower R_{ct}. This phenomenon is attributed to the positive "shielding effect" of the crystal water, which facilitates the solid-state diffusion of Na^+ ions. Meanwhile, the crystal water in between the layers facilitates the interfacial Na^+ ion transport.[29] When compared to the b-NMO with the post-physical mixture of CNTs and KBs, the b-NMO/C (the b-NMO supported by the carbon conductive networks) has more effective electron transport to deliver a higher b value and lower R_{ct}, which is beneficial to the enhancement of reaction kinetics.[47]

Galvanostatic charge and discharge curves were subsequently measured to evaluate the electrochemical performance. The charge–discharge curves of the b-NMO/C, b-NMO and b-NMO/C-HT cathodes at 0.25C are shown in Fig. S10a–c,† respectively. The curves show the quasi-linear plots without obvious plateaus, which are consistent with the CV results. The capacity of the b-NMO/C (192 mA h g^{-1}) is higher than those of b-NMO (176 mA h g^{-1}) and b-NMO/C-HT (121 mA h g^{-1}). The enhanced capacity of b-NMO/C is because of the effective electron transport networks and the facilitated interfacial Na^+ ion diffusion kinetics with a high b value and low R_{ct}.[48] Fig. 5a shows the rate performances of the b-NMO/C, b-NMO and b-NMO/C-HT in the range from 0.25 to 100C. Compared to the b-NMO and b-NMO/C-HT, the b-NMO/C exhibits highest capacity at each rate. In detail, the b-NMO/C delivers a capacity of 166 and 146 mA h g^{-1} at 0.5 and 1C, respectively. Surprisingly, even at higher rates of 10, 40 and 100C, it also retains a high capacity of 102, 70 and 43 mA h g^{-1}, respectively. The capacity from KBs and CNTs is only 0.08 and 0.003 mA h g^{-1} at 0.25C (Fig. S11†), indicating that the delivered capacity mainly comes from the layered oxides. A comparison of the rate capabilities of the state-of-the-art Mn-based SIB cathodes reported in the literature is shown in Fig. 5b.[49–55] The specific comparative data are shown in Table S4.† To the best of our knowledge, the b-NMO/C delivers better rate capability compared to the best reported results of Mn-based cathodes for sodium ion storage. Furthermore, long-life cycling performance and high coulombic efficiency at 25C (5 A g^{-1}) are subsequently exhibited in Fig. 5c. Compared to the b-NMO and b-NMO/C-HT, the b-NMO/C shows excellent cycling performance. In detail, the b-NMO/C exhibits the highest

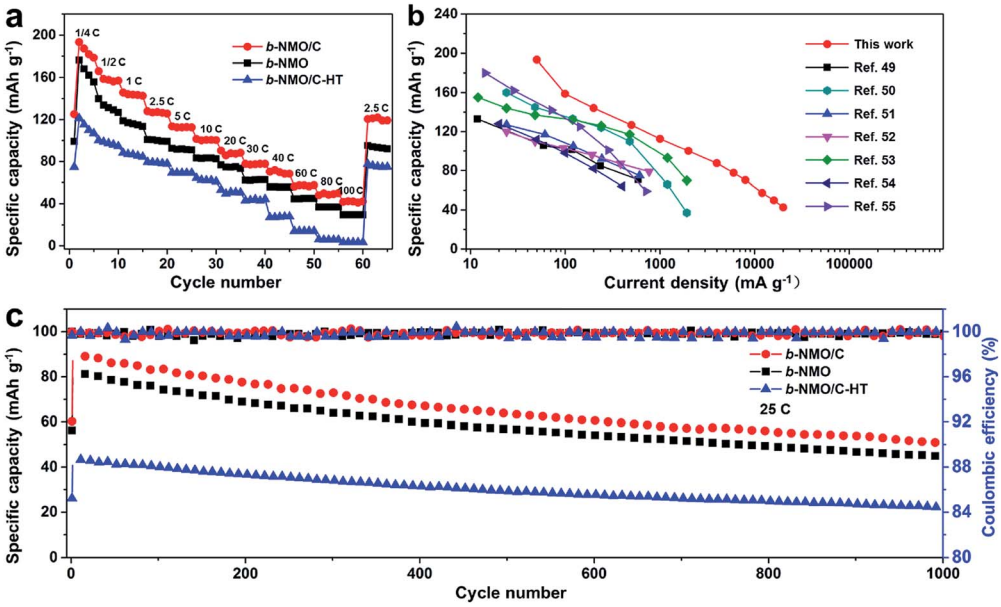

Fig. 5 (a) Rate performances of the b-NMO/C, b-NMO and b-NMO/C-HT at various rates from 0.25C to 100C. (b) A comparison of the rate capabilities of the state-of-the-art Mn-based cathodes for sodium ion batteries reported in the literature, P2-$Na_{0.8}[Li_{0.12}Ni_{0.22}Mn_{0.66}]O_2$ (ref. 49), $Na_{0.67}Mn_{0.80}Ni_{0.10}Mg_{0.10}O_2$ (ref. 50), P2-$Na_{0.45}Ni_{0.22}Co_{0.11}Mn_{0.66}O_2$ (ref. 51), P2-$Na_{0.66}Ni_{0.33-x}Zn_xMn_{0.67}O_2$ (Ref. 52), P2-$Na_{0.67}Mn_{0.65}Ni_{0.2}Co_{0.15}O_2$ (ref. 53), $Na_{0.67}[Mn_{0.65}Ni_{0.15}Co_{0.15}Al_{0.05}]O_2$ (ref. 54), P2-$Na_{0.5}[Ni_{0.23}Fe_{0.13}Mn_{0.63}]O_2$ (ref. 55). (c) Long-term cycling performances of the b-NMO/C, b-NMO and b-NMO/C-HT at a specific rate of 25C.

initial reversible capacity of 90 mA h g^{-1}. Notably, a very small capacity decay of 0.043% per cycle is obtained after 1000 cycles for the b-NMO/C, indicating relatively high capacity retention.

The rapid pseudocapacitive reaction leads to the remarkable rate performance of b-NMO/C, which is very promising as the cathode for SICs. Commercial graphite was used as the anode owing to the $[Na\text{-solvent}]^+$ co-intercalation behaviour which showed remarkable rate performance (Fig. S12b†)[56] and is able to match the rapid kinetics between the cathode and anode. According to the capacity balance between the b-NMO/C cathode and graphite anode (Fig. S10a and S12†), the mass ratio of cathode : anode is adjusted to 1 : 1.6, while the cathode is full sodiated previously. The as-assembled full SIC undergoes a large capacity loss at the first cycle (Fig. S13†) which may be due to the formation of the solid electrolyte interface (SEI) on the anode side (Fig. S12a†).[56] The capacity of SICs is calculated according to the total mass of both cathode and anode materials. The rate performance of the full SIC tested in the range of 0.5–3.8 V is shown in Fig. 6a. The specific discharge capacity of the SIC is 51 mA h g_{SIC}^{-1} at 0.1 A $g_{b\text{-}NMO/C}^{-1}$ (the specific current is given based on the mass of the cathode material). Eventually, the capacity is still 25 mA h g_{SIC}^{-1} at extremely high current densities (up to 8 A $g_{b\text{-}NMO/C}^{-1}$), indicating that the device is promising for achieving high rate capacity. The corresponding charge and discharge curves are shown in Fig. 6b, and the quasi-line discharge–charge curves exhibit the capacitive responses. The cycling stability was subsequently characterized (Fig. 6c). The capacity retention was 72% after 100 cycles, indicating good reversibility during the charge–discharge process. Further, energy density and power density are calculated. As shown in the Ragone plots (Fig. 6d), the b-NMO/C//graphite SIC delivers a maximum energy density of 91 W h kg^{-1} at a power density of 84 W kg^{-1}. When the power density is increased to 5816 W kg^{-1}, the energy density is 37 W h kg^{-1}. The b-NMO/C//graphite SIC shows a more remarkable performance than most of the reported state-of-the-art SICs, such as Nb_2O_5@C/rGO//AC,[3] TiO_2/GO//AC,[4] V_2O_5/CNT//AC,[6] and AC//AC.[57] The obtained data demonstrate that the as-assembled b-NMO/C//graphite SIC is a very promising energy storage device with high power and energy densities.

In summary, layered birnessite $Na_{0.77}MnO_2 \cdot 0.5H_2O$ supported by a two-dimensional conductive network (b-NMO/C) is synthesized by a low-cost wet-chemical method. The b-NMO/C shows the pseudocapacitive sodium storage behavior in non-aqueous systems, which is demonstrated for the first time. The sodium storage in the layered b-NMO/C cathode exhibited only ~2.4% layer expansion/shrinkage. Kinetic analysis shows that over 72.1% of the total capacity comes from a capacitive-controlled contribution, which enables ultrahigh-rate capability. As a sodium storage cathode, the b-NMO/C displays remarkable rate performance, delivering a capacity of 192 mA h g^{-1} at 0.25C and 102, 70 and 43 mA h g^{-1} at high rates of 10, 40 and 100C, respectively. The b-NMO/C shows stable cycling performance in the non-aqueous system. The as-assembled b-NMO/C//graphite SIC displays a maximum energy density of 91 W h kg^{-1} at a power density of 84 W kg^{-1}. When the power density is increased to 5816 W kg^{-1}, an energy density of 37 W h kg^{-1} is achieved. Our work proposes a facile and universal method to overcome the sluggish sodium ion and electron kinetics of layered transition metal oxide materials by introducing nanoconfined fluid water in between the layers for rapid ion diffusion and

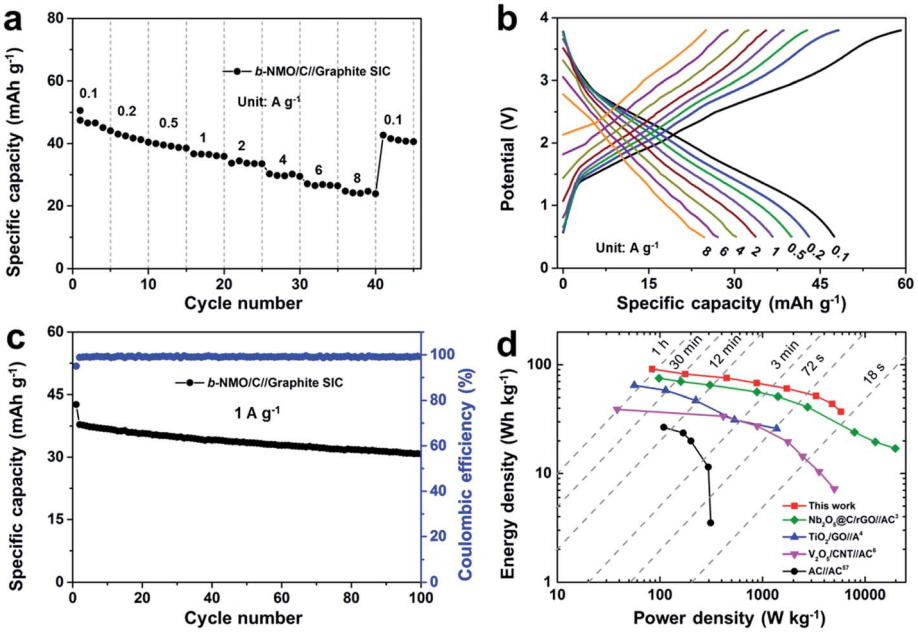

Fig. 6 Rate performances (a), charge/discharge curves (b) and cycling performance (c) of the b-NMO/C//graphite SIC. (d) Ragone plots of various full cells. The sodium ion capacitor based on b-NMO/C//graphite is compared with other SICs using Nb_2O_5@C/rGO//AC,[3] TiO_2/GO//AC,[4] V_2O_5/CNT//AC,[6] and AC//AC.[57]

constructing conductive networks for effective electron transport. We believe that this effective strategy provides a new insight into developing layered transition metal oxides for next generation SICs with both high energy and power density.

Conflicts of interest

There are no conflicts to declare.

Acknowledgements

This work was supported by the National Natural Science Fund for Distinguished Young Scholars (51425204), the National Natural Science Foundation of China (51521001, 51602239), the National Key Research and Development Program of China (2016YFA0202603, 2016YFA0202601), the National Basic Research Program of China (2013CB934103), the Programme of Introducing Talents of Discipline to Universities (B17034), the Hubei Provincial Natural Science Foundation of China (2016CFB267), the International Science & Technology Cooperation Program of China (2013DFA50840), the Fundamental Research Funds for the Central Universities (WUT: 2016III001, 2016III003, 2016IVA090, 2017III009, and 2017III005). The authors declare no competing financial interests.

Notes and references

1 B. E. Conway, *Electrochemical supercapacitors: scientific fundamentals and technological applications*, Kluwer-Academic, 1999.
2 V. Augustyn, P. Simon and B. Dunn, *Energy Environ. Sci.*, 2014, **7**, 1597–1614.
3 E. Lim, C. Jo, M. S. Kim, M. H. Kim, J. Chun, H. Kim, J. Park, K. C. Roh, K. Kang and S. Yoon, *Adv. Funct. Mater.*, 2016, **26**, 3553.
4 Z. Le, F. Liu, P. Nie, X. Li, X. Liu, Z. Bian, G. Chen, H. B. Wu and Y. Lu, *ACS Nano*, 2017, **11**, 2952.
5 H. K. Roh, M. S. Kim, K. Y. Chung, U. Mani, V. Aravindan, M. Srinivasan, K. C. Roh and K. B. Kim, *J. Mater. Chem. A*, 2017, **5**, 17506–17516.
6 Z. Chen, V. Augustyn, X. Jia, Q. Xiao, B. Dunn and Y. Lu, *ACS Nano*, 2012, **6**, 4319–4327.
7 D. Chao, C. H. Lai, P. Liang, Q. Wei, Y. S. Wang, C. Zhu, G. Deng, V. V. T. Doan-Nguyen, J. Lin and L. Mai, *Adv. Energy Mater.*, 2018, 1800058.
8 D. Chao, C. Zhu, X. Xia, J. Liu, X. Zhang, J. Wang, P. Liang, J. Lin, H. Zhang and Z. X. Shen, *Nano Lett.*, 2015, **15**, 565.
9 D. Xu, D. Chao, H. Wang, Y. Gong, R. Wang, B. He, X. Hu and H. J. Fan, *Adv. Energy Mater.*, 2018, 1702769.
10 P. He, H. Yu, D. Li and H. Zhou, *J. Mater. Chem.*, 2012, **22**, 3680–3695.
11 M. H. Han, E. Gonzalo, G. Singh and T. Rojo, *Energy Environ. Sci.*, 2014, **8**, 81–102.
12 P. F. Wang, Y. You, Y. X. Yin and Y. G. Guo, *Adv. Energy Mater.*, 2017, 1701912.
13 S. Guo, H. Yu, Z. Jian, P. Liu, Y. Zhu, X. Guo, M. Chen, M. Ishida and H. Zhou, *ChemSusChem*, 2014, **7**, 2115.
14 S. M. Oh, S. T. Myung, C. S. Yoon, J. Lu, J. Hassoun, B. Scrosati, K. Amine and Y. K. Sun, *Nano Lett.*, 2014, **14**, 1620–1626.
15 W. J. Li, C. Han, W. Wang, F. Gebert, S. L. Chou, H. K. Liu, X. Zhang and S. X. Dou, *Adv. Energy Mater.*, 2017, **7**, 1700274.
16 A. Caballero, L. Hernán, J. Morales, L. Sánchez, J. S. Peña and M. A. G. Aranda, *J. Mater. Chem.*, 2002, **12**, 1142–1147.
17 J. Billaud, R. J. Clément, A. R. Armstrong, z. J. Canales-Vã, P. Rozier, C. P. Grey and P. G. Bruce, *J. Am. Chem. Soc.*, 2015, **46**, 17243–17248.
18 N. Yabuuchi, M. Kajiyama, J. Iwatate, H. Nishikawa, S. Hitomi, R. Okuyama, R. Usui, Y. Yamada and S. Komaba, *Nat. Mater.*, 2012, **11**, 512.
19 Q. Wei, J. Liu, W. Feng, J. Sheng, X. Tian, L. He, Q. An and L. Mai, *J. Mater. Chem. A*, 2015, **3**, 8070–8075.
20 V. Augustyn and Y. Gogotsi, *Joule*, 2017, **1**, 443.
21 Q. An, Y. Li, H. D. Yoo, S. Chen, Q. Ru, L. Mai and Y. Yao, *Nano Energy*, 2015, **18**, 265–272.
22 D. Kundu, B. D. Adams, V. Duffort, S. H. Vajargah and L. F. Nazar, *Nat. Energy*, 2016, **1**, 16119.
23 M. Yan, P. He, Y. Chen, S. Wang, Q. Wei, K. Zhao, X. Xu, Q. An, Y. Shuang and Y. Shao, *Adv. Mater.*, 2018, **30**, 1.
24 K. W. Nam, S. Kim, S. Lee, M. Salama, I. Shterenberg, Y. Gofer, J. S. Kim, E. Yang, S. P. Chan and J. S. Kim, *Nano Lett.*, 2015, **15**, 4071.
25 E. A. Johnson and J. E. Post, *Am. Mineral.*, 2006, **91**, 609–618.
26 S.-D. Han, S. Kim, D. Li, V. Petkov, H. D. Yoo, P. J. Phillips, H. Wang, J. J. Kim, K. L. More and B. Key, *Chem. Mater.*, 2017, **29**, 4874.
27 H. Liu and K. Zhao, *J. Mater. Sci.*, 2016, **51**, 9306–9313.
28 X. Zhang, P. Yu, H. Zhang, D. Zhang, X. Sun and Y. Ma, *Electrochim. Acta*, 2013, **89**, 523–529.
29 A. Cormie, A. Cross, A. F. Hollenkamp and S. W. Donne, *Electrochim. Acta*, 2010, **55**, 7470–7478.
30 K. W. Nam, S. Kim, E. Yang, Y. Jung, E. Levi, D. Aurbach and J. W. Choi, *Chem. Mater.*, 2015, **27**, 150514111747006.
31 W. A. Ang, N. Gupta, R. Prasanth and S. Madhavi, *ACS Appl. Mater. Interfaces*, 2012, **4**, 7011.
32 G. Wang, L. Yi, R. Yu, X. Wang, Y. Wang, Z. Liu, B. Wu, M. Liu, X. Zhang and X. Yang, *ACS Appl. Mater. Interfaces*, 2017, **9**, 25358.
33 S. Bach, J. P. Pereira-Ramos and N. Baffier, *J. Power Sources*, 1997, **68**, 586–589.
34 M. Tsuda, H. Arai and Y. Sakurai, *J. Power Sources*, 2002, **110**, 52–56.
35 J. Luo, A. Huang, S. H. Park, S. L. Suib and C. O'Young, *Chem. Mater.*, 1998, **10**, 1561–1568.
36 D. S. Yang and M. K. Wang, *Chem. Mater.*, 2001, **13**, 2589–2594.
37 D. C. Golden, *Clays Clay Miner.*, 1987, **35**, 271–280.
38 M. C. Biesinger, B. P. Payne, A. P. Grosvenor, L. W. M. Lau, A. R. Gerson and R. S. C. Smart, *Appl. Surf. Sci.*, 2011, **257**, 2717–2730.
39 X. L. Wu, L. Y. Jiang, F. F. Cao, Y. G. Guo and L. J. Wan, *Adv. Mater.*, 2009, **21**, 2710–2714.

40 I. W. Kim, Y. Furukawa, T. L. Daulton, D. Lavoie and S. W. Newell, *Clays Clay Miner.*, 2003, **51**, 382–389.
41 S. Ko, J. I. Lee, H. S. Yang, S. Park and U. Jeong, *Adv. Mater.*, 2012, **24**, 4451–4456.
42 J. Desilvestro and O. Haas, *J. Electrochem. Soc.*, 1990, **137**, 5C–22C.
43 D. Chao, C. Zhu, P. Yang, X. Xia, J. Liu, J. Wang, X. Fan, S. V. Savilov, J. Lin and H. J. Fan, *Nat. Commun.*, 2016, **7**, 12122.
44 D. Sheberla, J. C. Bachman, J. S. Elias, C. J. Sun, S. H. Yang and M. Dincă, *Nat. Mater.*, 2017, **16**, 220.
45 J. Dong, Y. Jiang, Q. Li, Q. Wei, W. Yang, S. Tan, X. Xu, Q. An and L. Mai, *J. Mater. Chem. A*, 2017, **5**, 10827.
46 Y. Zhao, J. Feng, X. Liu, F. Wang, L. Wang, C. Shi, L. Huang, X. Feng, X. Chen and L. Xu, *Nat. Commun.*, 2014, **5**, 4565.
47 H. S. Kim, J. B. Cook, S. H. Tolbert and B. Dunn, *J. Electrochem. Soc.*, 2015, **162**, A5083–A5090.
48 S. Y. Lim, H. L. Ji, S. Kim, J. Shin, W. Choi, K. Y. Chung, D. S. Jung and J. W. Choi, *ACS Energy Lett.*, 2017, **2**, 998.
49 J. Xu, D. H. Lee, R. J. Clément, X. Yu, M. Leskes, A. J. Pell, G. Pintacuda, X. Q. Yang, C. P. Grey and Y. S. Meng, *Chem. Mater.*, 2014, **26**, 1260.
50 Z. Li, R. Gao, J. Zhang, X. Zhang, Z. Hu and X. Liu, *J. Mater. Chem. A*, 2016, **4**, 3453–3461.
51 D. Buchholz, A. Moretti, R. Kloepsch, S. Nowak, V. Siozios, M. Winter and S. Passerini, *Chem. Informationsdienst*, 2013, **44**, 142–148.
52 X. Wu, J. Guo, D. Wang, G. Zhong, M. J. Mcdonald and Y. Yang, *J. Power Sources*, 2015, **281**, 18–26.
53 Z. Y. Li, R. Gao, L. Sun, Z. Hu and X. Liu, *J. Mater. Chem. A*, 2015, **3**, 16272–16278.
54 D. Yuan, W. He, F. Pei, F. Wu, Y. Wu, J. Qian, Y. Cao, X. Ai and H. Yang, *J. Mater. Chem. A*, 2013, **1**, 3895–3899.
55 I. Hasa, D. Buchholz, S. Passerini, B. Scrosati and J. Hassoun, *Adv. Energy Mater.*, 2015, **4**, 1400083.
56 B. Jache and P. Adelhelm, *Angew. Chem.*, 2014, **53**, 10169–10173.
57 A. Burke, *Proc. IEEE Veh. Power Propulsion Conf. (VPPC'05)*, 2005, pp. 356–366.

